

See discussions, stats, and author profiles for this publication at: <https://www.researchgate.net/publication/351475223>

Active disturbance rejection control of layer width in wire arc additive manufacturing based on deep learning

Article in Journal of Manufacturing Processes · May 2021

DOI: 10.1016/j.jmapro.2021.05.005

CITATIONS

8

READS

209

8 authors, including:



Yiming Wang

Nanjing University of Science and Technology

6 PUBLICATIONS 28 CITATIONS

[SEE PROFILE](#)



Jun Lu

Nanjing University of Science and Technology

15 PUBLICATIONS 34 CITATIONS

[SEE PROFILE](#)



Zhuang Zhao

Nanjing University of Science and Technology

42 PUBLICATIONS 138 CITATIONS

[SEE PROFILE](#)



Wenxiang Deng

Nanjing University of Science and Technology

50 PUBLICATIONS 1,280 CITATIONS

[SEE PROFILE](#)

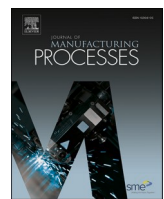
Some of the authors of this publication are also working on these related projects:



Project Nonlinear Control of Electro-Hydraulic Servo Systems [View project](#)



Project Active disturbance rejection control of layer width in wire arc additive manufacturing based on deep learning [View project](#)



Active disturbance rejection control of layer width in wire arc additive manufacturing based on deep learning

Yiming Wang^{a,1}, Jun Lu^{a,1}, Zhuang Zhao^{a,*}, Wenxiang Deng^{b,*}, Jing Han^a, Lianfa Bai^a, Xiaowei Yang^b, Jianyong Yao^b

^a Jiangsu Key Laboratory of Spectral Imaging and Intelligent Sense, Nanjing University of Science and Technology, Nanjing, 210094, China

^b School of Mechanical Engineering, Nanjing University of Science and Technology, Nanjing, 210094, China



ARTICLE INFO

Keywords:
Additive manufacturing
Deep learning
Semantic segmentation
ADRC
Feedback control

ABSTRACT

In the process of wire arc additive manufacturing (WAAM), in order to improve the welding quality, the width of deposited layer needs to be monitored, and a feedback control strategy for the width of deposited layer must be developed. In this study, the feedback control of layer width based on melt pool vision was realized in WAAM process. The vision sensing system is used to collect the melt pool image during the welding process, and the weld width is determined according to the segmentation network EPNet designed. Finally, an active disturbance rejection control (ADRC) algorithm was designed to achieve real-time control of the melt pool width during welding. The experimental results show that the designed control algorithm can guarantee satisfactory control accuracy of melt pool width, which provides necessary strategies for online monitoring and control of weld width during WAAM.

1. Introduction

Additive manufacturing (AM) is a new manufacturing technology developed in 1980s, which has provided a new potential direction for modern manufacturing industry. Additive manufacturing directly accumulates materials layer by layer into desired components [1–3], rather than reducing raw materials like traditional manufacturing methods. AM can quickly and accurately manufacture objects with complex shapes, and has the advantages of simple structure, low technology cost and high production efficiency [4]. It has been widely used in automobile [5], aerospace [6], medical [7] and other industrial fields [8].

Metal AM is divided into four categories, namely powder bed fusion, material injection, binder injection and direct energy deposition [9]. WAAM is a process in which the welding arc is used as the energy to melt metal wire, and metal wire is continuously melted and accumulated. WAAM has the advantages of environmental protection, low equipment cost and high deposition rate. It has broad application prospects in aerospace [10], shipbuilding [11], construction [12] and other industries. However, in the WAAM process, as layer number increased, problems will occur in deposited layer [13], such as severe accumulation

of heat, poor heat dissipation conditions, slowly solidified melt pool, and difficult to control deposited layer shape. In addition to these internal problems, the interference of the external environment such as airflow, air humidity and oil pollution will also affect the metallurgical bonding strength, dimensional accuracy and surface accuracy of the deposited layer. In fact, the dimension and quality of molding single-bead deposition directly determine the forming quality of the stacked components, because the deposited component is composed of a series of single-bead deposition. Therefore, it is necessary to develop a real-time feedback system to monitor and control the forming quality and stability of the WAAM deposition process.

In recent years, with the promotion from academics and industries, the combination of imaging technology and deep learning has been extensively investigated in many fields [14]. Vision-based melt pool monitoring systems have been gradually applied in the welding process [15]. A melt pool monitoring system allows to observe the shape of the melt pool in real time to provide reliable feedback of the welding process. Du et al. [16] used optical sensing technology to record the weld bead image, and then calculated the three-dimensional (3D) shape parameters of the weld, so as to realize the automatic detection of the 3D shape of a weld bead. Shen et al. [17] established a passive dual path

* Corresponding authors.

E-mail addresses: zhaozhuang@njust.edu.cn (Z. Zhao), wxdeng_njust@163.com (W. Deng).

¹ These authors contributed equally to this work.

melt pool vision sensing system and determined the best band for capturing melt pool images. An improved LeNet deep network is proposed to classify different welding speeds and monitor welding stability. The model has high classification accuracy and fast response speed. Wu et al. [18] used the keyhole visual signal to monitor the weld penetration, and controlled the variable polarity plasma arc welding process by adjusting the welding current and plasma gas flow rate to obtain a full-penetrated weld. Kwon et al. [19] applied a deep neural network to selective laser melting, and studied a classification model of melt pool images under different laser power labels. The classification model can be used to infer the location to cause the unexpected alteration of microstructures or separate the defective products non-destructively. Huang et al. [20] developed a vision sensor system using 3D and two-dimensional (2D) visual information fusion methods, which has high accuracy and resolution for obtaining narrow seam information. Bacioiu et al. [21] studied a vision system composed of a high dynamic range (HDR) camera, combined with a new adaptive neural network classification paradigm, and proposed a model for identifying welding defects, which achieved high accuracy.

Although the research on WAAM is gradually increasing, the research direction is not absolutely comprehensive. Researchers pay more attention to issues such as path planning, microstructure evolution and process simulation. In the WAAM process, higher requirements are also placed on the geometry of the components, which requires strengthening the feedback control strategies for layer geometry. However, the results and insights of the WAAM process monitoring and control work are still sparse, and have not been compiled in a single source [22]. Li et al. [23] proposed an adaptive process control scheme to maintain a uniform bead geometry. As this approach is an open-loop control system, high accuracy modelling of the process is required. Xiong et al. [24] designed an intelligent single-neuron self-adjusting controller for variable layer width control in WAAM, which can effectively improve the stability of the process. Xia et al. [25] proposed to use model predictive control (MPC) to control the layer width of the WAAM process. The controller has good tracking performance, and its robustness is better than traditional PID controller, and it has reached acceptable accuracy. Liu et al. [26,27] controlled the weld penetration and 3D weld pool surface by utilizing the 3D weld pool sensing system and characterization of the weld pool surface. The developed control system can effectively realize the desired weld joint penetration and the 3D weld pool surface geometry under various disturbances and initial conditions. Most of the above methods are based on traditional methods, and it is difficult to adequately mine the link between monitoring and control variable. In addition, the traditional methods have poor robustness and are difficult to adapt to complex working conditions. However, deep learning can extract deeper feature information, which can better dig out the inner link with the control variable, and improve the effect of WAAM monitoring and control.

Therefore, this paper proposes an ADRC strategy based on the layer width control of deep learning in WAAM. It uses the visual information of melt pool to monitor and control the width of each cladding layer in the WAAM process in real time. To facilitate the ADRC design, a second-order control model is obtained by identifying the relationship between the welding current and the width of the weld pool. The deviation between the identified model and the real system is considered as the generalized disturbance. In the designed ADRC framework, a linear extended state observer (ESO) is constructed to estimate the unknown system state and disturbance. Then the estimated state is employed to design the output feedback controller only based on the melt pool width information. Also, the estimated disturbance is adopted to achieve the active disturbance feedforward compensation, which strengthens the robustness of the system against additive disturbances and further facilitates the improvement of the control accuracy of the melt pool width. The closed-loop system stability analysis indicates that the designed ADRC ensures the actual weld pool width can well track the reference width. The final results verify the effectiveness of designed control

algorithm.

This paper is organized as follows. In Section 2, the visual acquisition system of melt pool is introduced. In Section 3, the network structure of EPNet and the extraction method of melt pool width are introduced in detail. The detailed design and simulation validation of ADRC algorithm are presented in Section 4. Section 5 presents the relevant experiments and analyzes the results. Section 6 summarizes this paper.

2. Experiment system

The experimental system is shown in Fig. 1. It consists of an ABB robot (IRB 2600), a Fronius welder (4000-R), a control cabinet (IRC5 Single), a vision sensing system, and a computer for control. The vision sensing system includes a charge coupled device (CCD) camera (Basler ace acA1920-155um) and a computer.

The camera is fixed on the robot arm of the ABB robot, and the angle between it and the welding torch is 40°. In order to eliminate the interference of redundant band radiation during acquisition, 850 nm high-pass filter and protective glass are set in the front of CCD. The melt pool is a pool-like liquid area formed by the molten metal dripping on the base material, and the width of melt pool is measured with a CCD camera. The robot control cabinet is used to adjust the welding process and control the movement of robot. The weld width is extracted from melt pool image, and the welding current can be adjusted in real time by changing the simulated input of welding machine.

To shorten the calculation, the region of interest (ROI) is extracted. Then EPNet is used to segment the melt pool image, detect melt pool edge and extract weld width. The flow chart of weld width extraction is shown in Fig. 2. The camera is calibrated, and the relationship between the number of pixels in the image and the width of the real world in the melt pool is obtained. The actual width of a single pixel is 0.07 mm. Therefore the actual width of melt pool can be calculated as the following equation.

$$Width_{actual} = 0.07 \times Width_{img} \quad (1)$$

3. Modeling method

By obtaining the contour of melt pool and analyzing it, the welding process can be controlled and the welding quality can be effectively improved. Ma et al. [28] made improvements on Otsu threshold segmentation method. Yu et al. [29] used an improved contour extraction algorithm based on Canny in defect detection of steel plates. Chen et al. [30] improved the gradient operator and applied it to contour extraction of high temperature solidified metals. However, during the welding process, the real-time image of melt pool will be disturbed by smoke and arc reflections, which will seriously damage the image quality [31]. The results of the traditional edge detection algorithm are shown in Fig. 3. It is difficult to accurately extract the contour of melt pool image, which contains many smoke regions.

In recent years, with the rapid development of deep learning, it has been widely used in various industrial fields [32–34], especially in the field of welding. As an important part of computer vision, many researchers have contributed to the development of semantic segmentation and obtained valuable results. The main semantic segmentation networks are: FCN [35], SegNet [36], ENet [37], ErfNet [38], etc. They can achieve better results in semantic segmentation tasks [39].

Image-based semantic segmentation is also understood as dense pixel prediction, in which each pixel is classified. Fully Convolutional Network (FCN), as a classic of semantic segmentation networks in deep learning, converts the fully connected layers of traditional classification networks into convolutional layers. Then through deconvolution for upsampling, gradually restore the detailed information of image and expand the size of feature map. In the process of restoring detailed information of image, FCN is not only realized by using deconvolution. The skip-connection method is also used to fuse the feature information

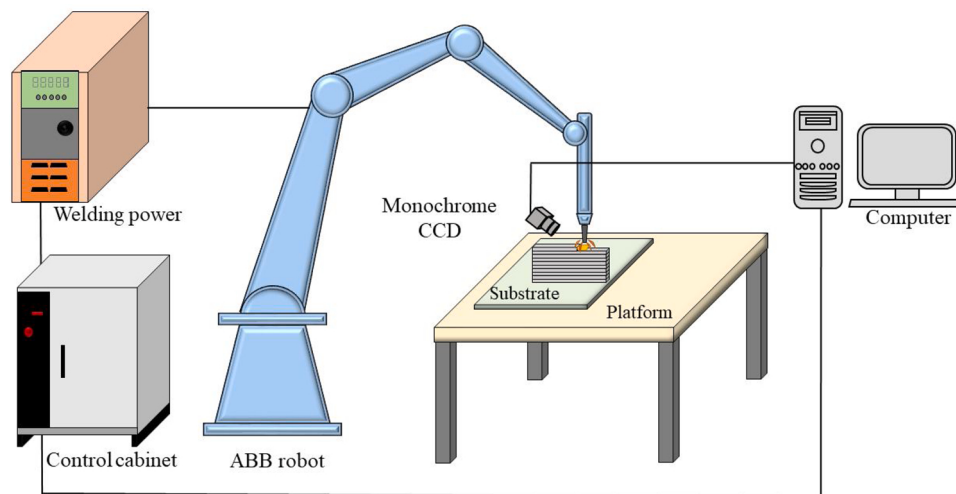


Fig. 1. Schematic diagram of the WAAM system.

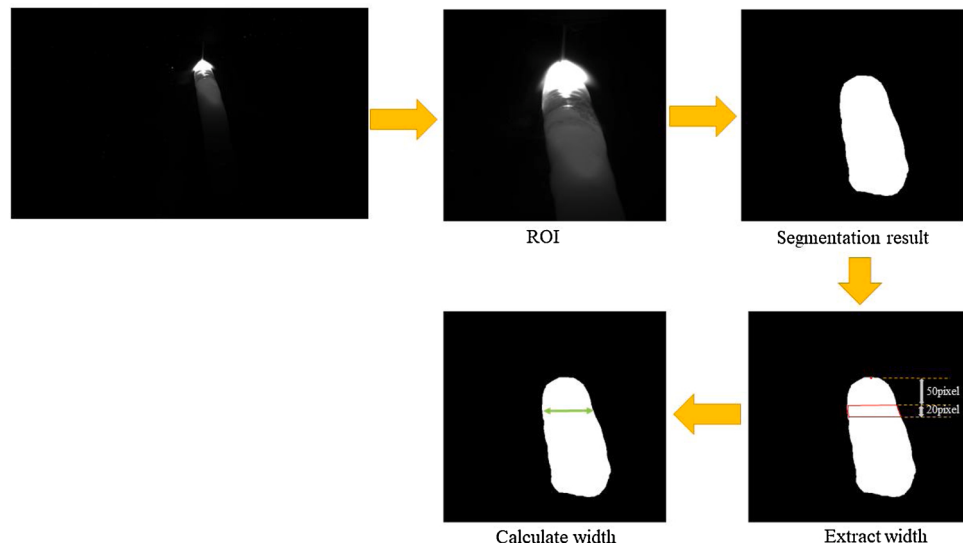


Fig. 2. Flow chart of weld width extraction.

obtained in the downsampling process with the corresponding feature map during the upsampling process. However, there is semantic information loss in FCN, and there is a lack of research on the correlation between pixels. SegNet adopts the encoder-decoder structure of FCN, but it is different from FCN. SegNet does not use skip-connection structure, and in the process of upsampling, unpooling is used instead of deconvolution. Compared with FCN, the number of SegNet parameters decreases and the integrity of high-frequency information is guaranteed. However, when unpooling the feature map of lower resolution, the information between the neighbors of the pixel is also ignored. ENet is a lightweight real-time segmentation network based on SegNet. The original intention of ENet design is how to minimize the amount of calculation and increase the calculation speed, so the accuracy requirements are not high. The purpose of ERFNet is to improve the accuracy and speed at the same time, which can be regarded as the improvement of ENet. ERFNet uses residual connections to accelerate feature learning and eliminate the phenomenon of gradient disappearance in a stacked network structure. In addition, depthwise separable convolution is used, which can reduce the number of parameters in the network, improve training efficiency and actual calculation speed. Considering the actual engineering application requirements, this paper uses ERFNet as the basic network of melt pool segmentation.

The vision sensing system collects molten pool image with a size of 1920×1200 pixels. Because the melt pool area occupies a small proportion in the collected images, this paper takes melt pool area as center, and crops collected image with 512×512 pixel ROI. The contour of melt pool region is extracted manually from the image and converted into a binary image in the dataset as a label. Because traditional edge detection algorithms cannot accurately identify both ends of the melt pool, to ensure accuracy of label, this paper uses Photoshop and MATLAB to make the label. The cropped image and the corresponding label are shown in Fig. 4.

3.1. Network structure

As shown in Fig. 5(a), the network designed in this paper follows the encoder-decoder structure of ErfNet. At the same time, the encoder part is composed of non-bottleneck-1D and downsampling modules. The Decoder part consists of upsampling and non-bottleneck-1D modules. Among them, non-bottleneck-1D is a network structure using residual connections, as shown in Fig. 6(b) [38].

The composition of classic residual block is shown in Fig. 6(a) [40]. If some layers are directly fitted to a potential identity mapping function $H(x) = x$, it is more difficult. The network is designed as $H(x) = F(x) +$

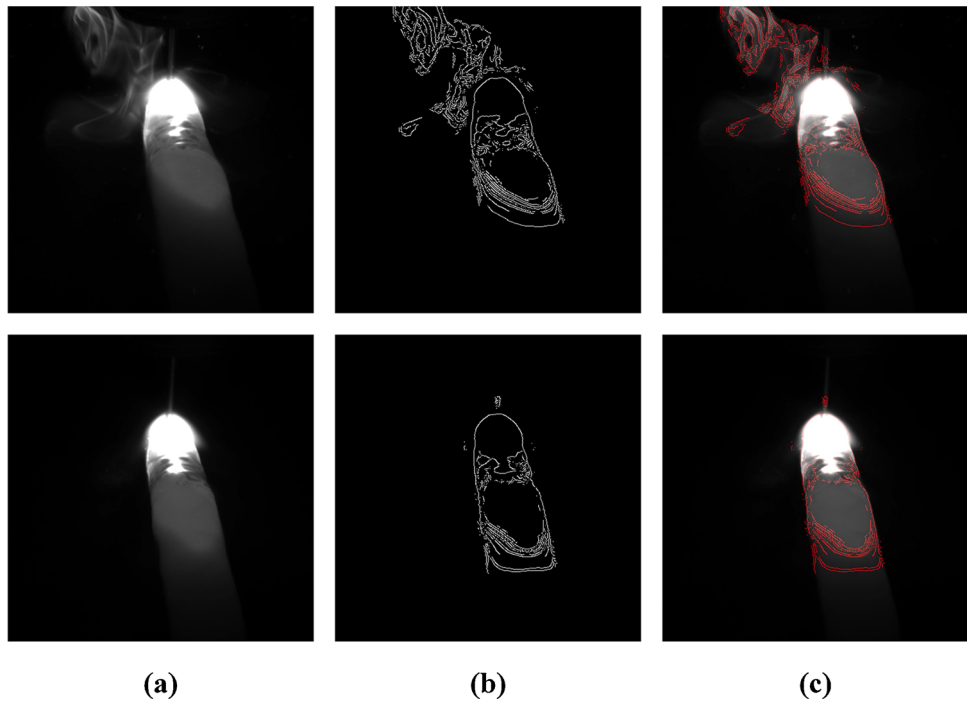


Fig. 3. The effect of traditional contour extraction algorithms: (a) original image; (b) contour image; (c) contour superimposed on melt pool image.

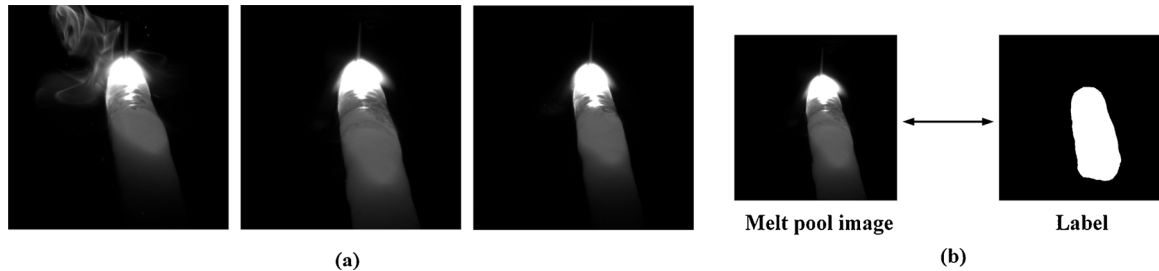


Fig. 4. (a) Cropped images of different melt pools; (b) Image of melt pool and corresponding label.

x . It can be converted to learning a residual function $F(x) = H(x) - x$. The residual structure makes the network not fit the original mapping, but fit the residual mapping, which reduces the learning difficulty by directly passing the input information to the output through skip connection. When the residual $F(x) = 0$, the accumulation can also serve as an identity map, and learning an all-zero matrix is much easier than learning an identity matrix. Deep residual network solves the problem of network degradation. Commonly, $F(x) > 0$, therefore, new features can always be learned through the network, which improves the network performance.

In Non-bottleneck-1D, dilated convolution [41] is interleaved to enable the network to obtain more context information. Downsample is all a set of parallel maxpooling and convolution operations. Non-bottleneck-1D has fewer parameters and faster speed than residual block. At the same time, it maintains the learning ability and accuracy equivalent to the non-bottleneck design.

In order to make the melt pool segmentation network EPNet obtain a better contour extraction effect, the pyramid pooling module (PPM) is added to the backbone network, as shown in Fig. 5(b).

PPM is a module proposed in semantic segmentation network PSPNet [42]. It solves the problem that network cannot effectively fuse the global feature information. PPM divides the feature map extracted from the previous network into two branches. A branch is divided into multiple sub-regions (the PPM in this paper is 4 layers, and the size of each layer is 1×1 , 2×2 , 3×3 , 6×6), and global average pooling

(GAP) is performed. Then use 1×1 convolution to adjust channel size to reduce the channel to original $1/N$, where N is 4. The size before pooling is obtained by upsampling each feature map using bilinear interpolation. Finally, the two branches (original feature map and feature map obtained by upsampling) are concatenated. PPM can aggregate the context of different regions to achieve the purpose of obtaining global context.

Taking the three-channel RGB image with a resolution of 512 pixel \times 512 pixel divided into class C as an example, the specific network structure of EPNet is shown in Table 1.

In addition, the loss function uses cross entropy loss function commonly used in semantic segmentation. For each category, our predicted probabilities are p and $1 - p$. The formula is as follows:

$$\text{Loss} = \frac{1}{N} \sum_i -[y_i \cdot \log(p_i) + (1 - y_i) \cdot \log(1 - p_i)] \quad (2)$$

where, y_i represents the label of sample i , positive class is 1, and negative class is 0. p_i represents the probability that sample i is predicted to be positive. N represents the number of categories.

3.2. Degenerate learning rate to prevent over fitting

In deep learning, the learning rate determines whether the parameters can be moved to the optimal value, and the speed of the movement. A proper learning rate can make the target parameter reach the optimal

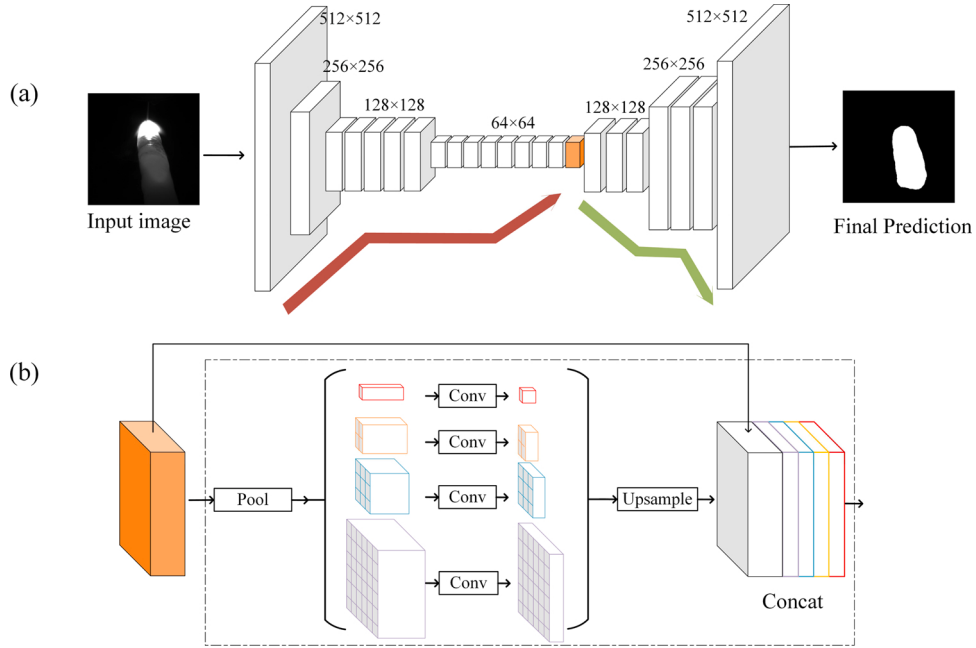


Fig. 5. Network structure (a) EPNet; (b) Pyramid Pooling Module.

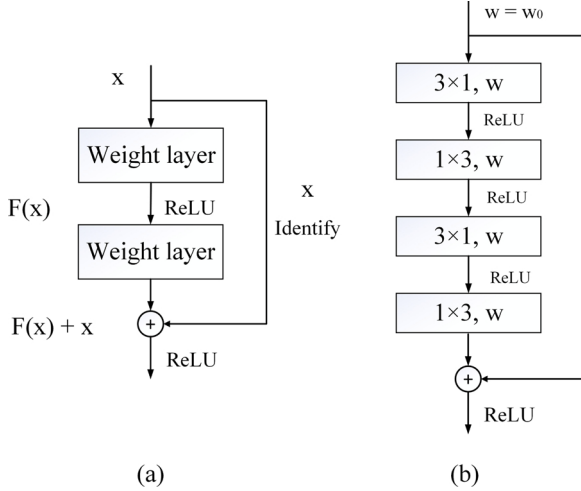


Fig. 6. (a) Residual block; (b) Non-bottleneck-1D.

value as soon as possible. When solving the minimum value of problem by stochastic gradient descent, it is necessary to find an appropriate gradient [43].

If learning rate is too large, it is easy to appear the phenomenon of gradient explosion. That is, in the process of gradient descent, the extremum points diverge, or take the form of oscillation similar to periodic function, resulting in gradient explosion. On the contrary, if the value of learning rate is too small, it will be difficult for the algorithm to find the optimal descent direction. In other words, the optimal solution cannot be found when wandering at a saddle point. After many iterations, the loss still fails to converge to the minimum [44].

In view of the above situation, the method of degenerate learning rate is adopted to set the learning rate. Degenerate learning rate is also called attenuated learning rate, and its principle is as follows: In the initial training, the large learning rate is used to accelerate training of network model. In later training, the learning rate is reduced to seek the optimal solution and improve classification accuracy [45]. The formula is as follows:

Table 1
Layer disposal of EPNet.

Layers	Type	Output size
1	Downsample block	16 × 256 × 256
2	Downsample block	64 × 128 × 128
3–7	5×Non-bottleneck-1D	64 × 128 × 128
8	Downsample block	128 × 64 × 64
9	Non-bottleneck-1D (dilated 2)	128 × 64 × 64
10	Non-bottleneck-1D (dilated 4)	128 × 64 × 64
11	Non-bottleneck-1D (dilated 8)	128 × 64 × 64
12	Non-bottleneck-1D (dilated 16)	128 × 64 × 64
13	Non-bottleneck-1D (dilated 2)	128 × 64 × 64
14	Non-bottleneck-1D (dilated 4)	128 × 64 × 64
15	Non-bottleneck-1D (dilated 8)	128 × 64 × 64
16	Non-bottleneck-1D (dilated 16)	128 × 64 × 64
17	Pyramid Pooling Module	128 × 64 × 64
18	Deconvolution(upsampling)	64 × 128 × 128
19–20	2×Non-bottleneck-1D	64 × 128 × 128
21	Deconvolution(upsampling)	16 × 256 × 256
22–23	2×Non-bottleneck-1D	16 × 256 × 256
24	Deconvolution(upsampling)	C×512 × 512

$$DLR = \eta \times \gamma^{\frac{n}{m}} \quad (3)$$

where, η is the original set learning rate; γ is attenuation rate; n is the number of cycles; m is the number of attenuation intervals. This method not only speeds up the convergence speed of network model, but also prevents the occurrence of over fitting and improves classification accuracy.

3.3. Data augmentation

The experiment is based on NVIDIA RTX 2080Ti graphics card and Pytorch deep learning architecture. The actual melt pool data required is obtained by welding, 500 images and corresponding labels are used as the training set, and the other 100 images and corresponding labels are used as the test set.

This paper uses a semantic segmentation network to get the width of melt pool. Due to the complexity and high requirements of the welding process, the number of data sets obtained is small, and the

generalization ability of model directly trained in practical applications is weak. To solve the problem, the data augmentation of dataset before the data is transmitted to network can greatly improve the data utilization rate, so that the network model can obtain stronger edge extraction capabilities and improve the robustness. The operation flow of data augmentation is shown in Fig. 7. The process includes rotation, scaling and cropping of the melt pool image and label, and the use of random numbers to adjust the intensity of the operation to increase the randomness of the data.

The following is the specific data augmentation process:

- (1) Randomly generate a floating number M between 0 and 1, and set $R = 2 \times M - 1$. According to the set maximum rotation angle θ , maximum zoom factor s , maximum crop length h and width w , multiply by R to control the intensity of shape change. Brightness, contrast, sharpness, Gaussian blur and other transformations are controlled by a randomly generated floating number ranging from 0 to 5;
- (2) Rotate and scale the data. If R is greater than or equal to 0, crop image and label. If R is less than 0, do not perform this operation;
- (3) Input the augmented data into the EPNet network for training.

3.4. Evaluation index

To quantitatively evaluate the accuracy of semantic segmentation results, mean intersection over union (MIOU) is used as the evaluation index. The formula is as follows:

$$MIoU = \frac{1}{k+1} \sum_{i=0}^k \frac{TP}{TP + FP + FN} \quad (4)$$

where TP , FP and FN are respectively the number of true positives, false positives and false negatives at pixel level. $k+1$ is the category. The results of testing different networks are shown in Table 2. It proves the effectiveness of EPNet and DA strategies.

As can be seen from Table 2 that test accuracy of EPNet is 2.69 % higher than that of ERFNet without using data augmentation. After using the data augmentation strategy, the test accuracy of EPNet is increased by 1.82 %.

The width extraction process is shown in Fig. 2. We take the first pixel at the front of the melt pool of segmentation result as reference, and the average width of the 50–70th pixel area under the orientation is used as the weld width.

4. Active disturbance rejection controller design

4.1. System identification

To improve the welding width control accuracy, proper control model which describes the major dynamic characteristics of the system should be first established. For the WAAM process, the welding current has the most obvious effect on welding width. Hence, welding current is selected as system input and system output is welding width. To obtain

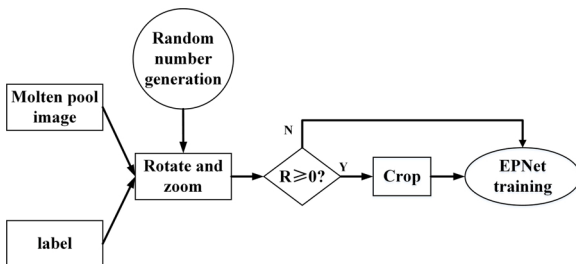


Fig. 7. Flow chart of data augmentation process.

Table 2

Test accuracy of different networks.

	ERFNet	EPNet	EPNet + DA
Accuracy	89.67 %	92.36 %	94.18 %

the dynamic model of the welding process, a step-response experiment was conducted for system identification. For additive manufacturing step-response experiment, the current is changed in the fifth layer. The welding parameters can be seen from Table 3.

Case 1: the current from 175A to 195A when $x = 300$. As shown in Fig. 8.

Case 2: the current from 175A to 159A when $x = 300$. As shown in Fig. 9

Based on the step-response experiment data, the following second-order transfer function can be utilized to approximate the relationship between the welding current and the width.

$$G(s) = \frac{k_p}{(T_{p1}s + 1)(T_{p2}s + 1)} \quad (5)$$

where $k_p > 0$ represents the welding current gain; T_{p1} and T_{p2} represent time constants of the second-order system in (5), respectively. Selecting the group with the best fitting effect, namely the fourth group of data, we can obtain $k_p = 0.0347$, $T_{p1} = 1.0886$ and $T_{p2} = 0.001$ by system identification.

Since the deviation between the identified model and the actual system is unavoidable, it is considered as the disturbance of the identified model. Then, the state-space expression of the system (5) is given by

$$\begin{cases} \dot{x}_1 = x_2 \\ \dot{x}_2 = k_p u/a - bx_2/a - x_1/a + f(t)/a \end{cases} \quad (6)$$

where x_1 represents the width of the welding pool and x_2 is its time derivative; $a = T_{p1}T_{p2}$ and $b = T_{p1} + T_{p2}$; the disturbance $|f(t)| < \delta$ and δ is a positive constant.

Based on the system state space Eq. (6), we design an active disturbance rejection controller to improve the welding quality. The block diagram of ADRC was presented in Fig. 10.

4.2. Extended state observer (ESO) design

Our control attempt is to make the actual welding width can track the desired width of the welding pool as accurately as possible. To design the control input u that represents the welding input current in practice, we define $x_3 = f(t)/a$ and $\dot{x}_3 = h(t)$. Hence, the extended state-space expressions can be constructed as:

$$\begin{cases} \dot{x}_1 = x_2 \\ \dot{x}_2 = k_p u/a - bx_2/a - x_1/a + x_3 \\ \dot{x}_3 = h(t) \end{cases} \quad (7)$$

In order to design the active disturbance rejection controller, a linear ESO is constructed to acquire the estimations of unknown system state and disturbance. By referring to [46], the linear ESO can be constructed as:

Table 3

Experimental parameters of WAAM.

Parameters	Value
Welding speed	7 mm/s
Ar (98.5 %) and O ₂ (1.5%) gas flow	25 L/min
Welding wire	ER316L
Wire electrode diameter	1.2 mm
Base material	304 stainless steel
Welding length	100 mm
CCD acquisition frequency	100 Hz
Exposure time	200 μs

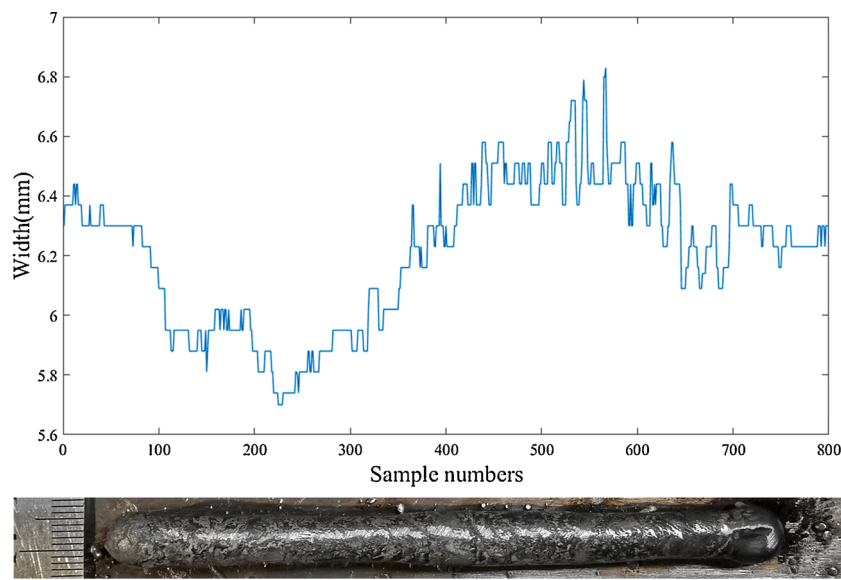


Fig. 8. Step-response experimental results of current from 175A to 195A.

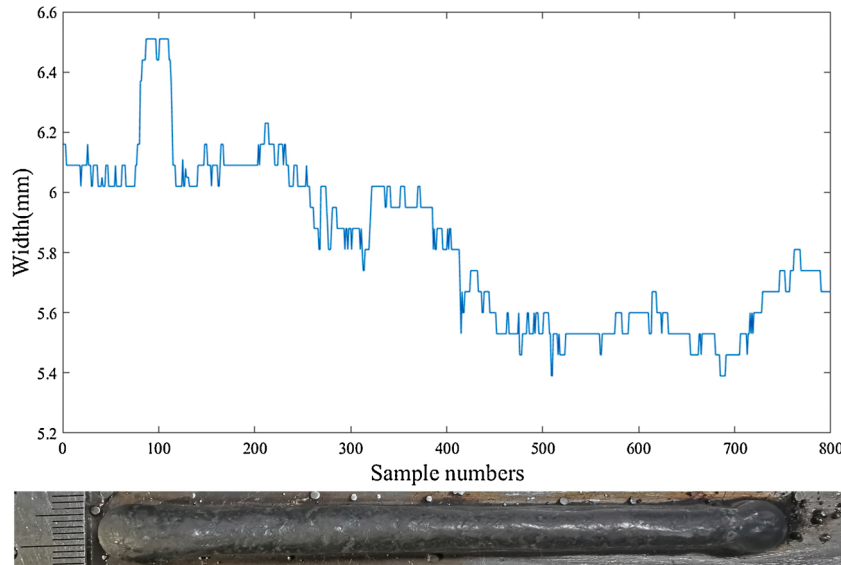


Fig. 9. Step-response experimental results of current from 175A to 159A.

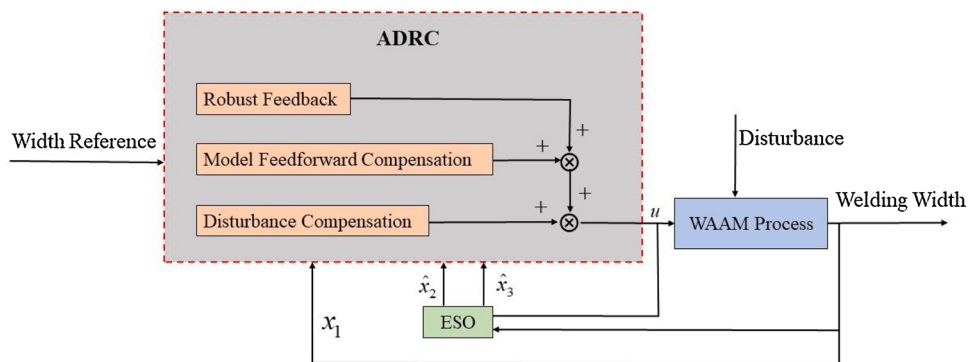


Fig. 10. Block diagram of ADRC.

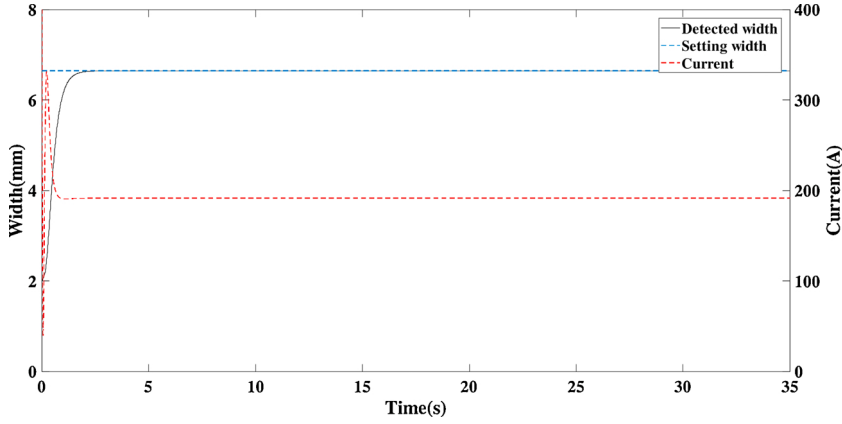
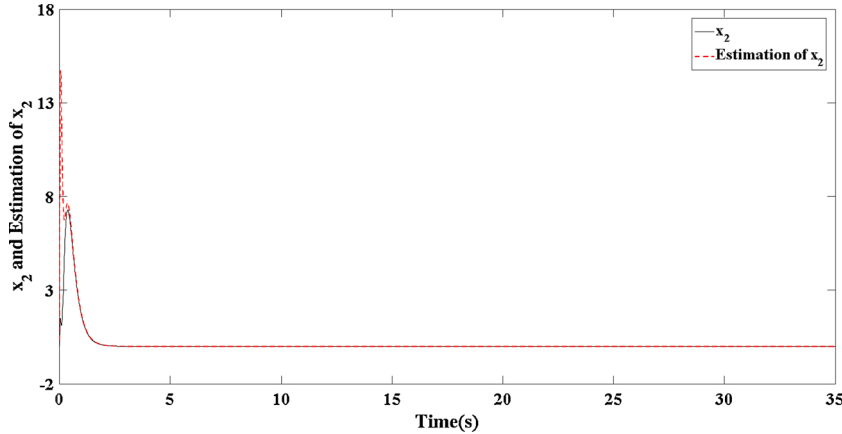


Fig. 11. Tracking trajectory and control current without disturbances.

Fig. 12. x_2 and estimation of x_2 without disturbances.

$$\left\{ \begin{array}{l} \dot{\hat{x}}_1 = \hat{x}_2 - 3w_0(\hat{x}_1 - x_1)\dot{\hat{x}}_2 = k_p u / a - b\hat{x}_2 / a - \hat{x}_1 / a + \hat{x}_3 - 3w_0^2(\hat{x}_1 \\ \quad - x_1)\dot{\hat{x}}_3 \\ = -w_0^3(\hat{x}_1 - x_1) \end{array} \right. \quad (8)$$

where w_0 is the bandwidth of ESO.

According to (7) and (8), the dynamic of the state estimation error of ESO can be written as:

$$\dot{\xi} = w_0 A \xi + M + B \frac{h(t)}{w_0^2} \quad (9)$$

where $\xi = [\xi_1, \xi_2, \xi_3]^T = [\tilde{x}_1, \frac{\tilde{x}_2}{w_0}, \frac{\tilde{x}_3}{w_0}]^T$; $\tilde{\bullet}$ represents the estimation error of \bullet ; $B = [0; 0; -1]$, $M = [0; (-b\tilde{x}_2/a - \tilde{x}_1/a + \tilde{x}_3)/w_0; 0]$ and $A =$

$$\begin{bmatrix} -3 & 1 & 0 \\ -3 & 0 & 1 \\ -1 & 0 & 0 \end{bmatrix}.$$

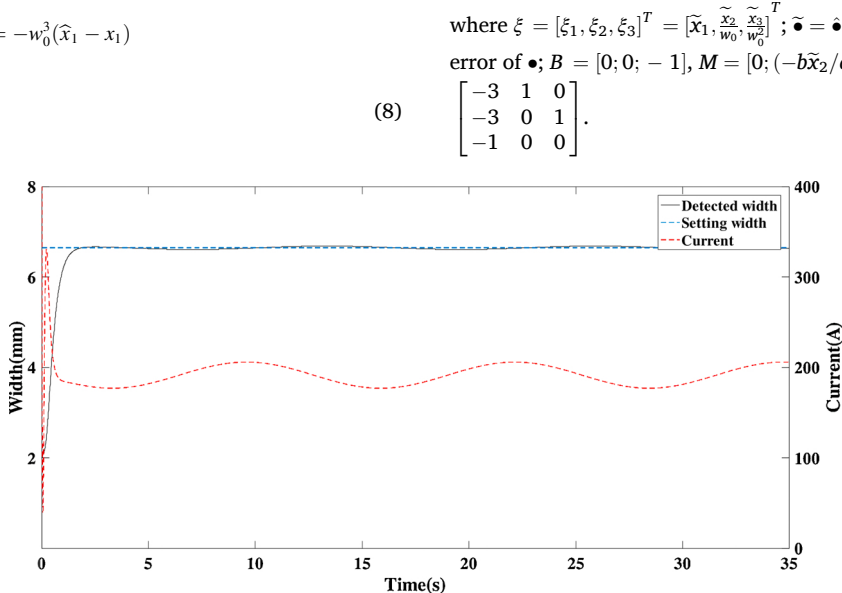


Fig. 13. Tracking trajectory and control current with disturbances.

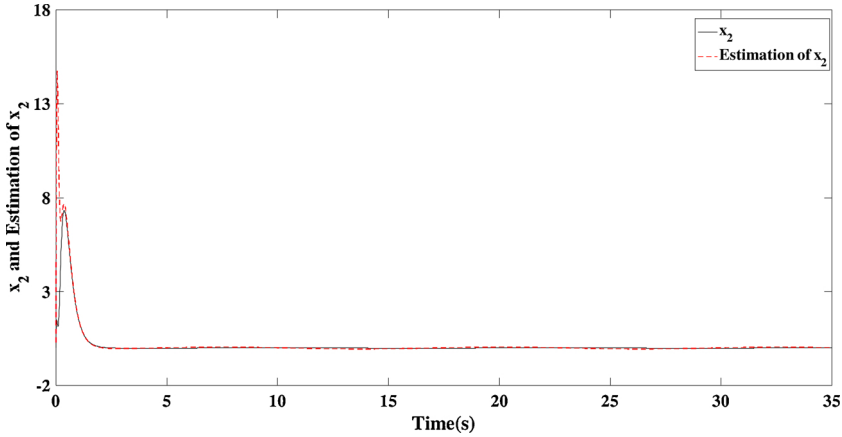


Fig. 14. x_2 and estimation of x_2 with disturbances.

Since the matrix A is Hurwitz, there exists a positive definite matrix P , which satisfies the following Lyapunov equation:

$$PA + A^T P = -I_{3 \times 3} \quad (10)$$

where $I_{3 \times 3}$ represents an identity matrix. Hence, according to [47], it can be deduced that the designed ESO in (8) is asymptotically stable.

4.3. Controller design

In order to accomplish the active disturbance rejection controller design, define a set of variables as follows:

$$\begin{cases} z_1 = x_1 - x_{1d} \\ \hat{z}_1 = \hat{x}_2 - \dot{x}_d \\ z_2 = \dot{z}_1 + k_1 z_1 = x_2 - x_{2eq} \\ x_{2eq} = \dot{x}_d - k_1 z_1 \\ \hat{z}_2 = \hat{x}_2 - x_{2eq} \end{cases} \quad (11)$$

where x_{1d} is the desired welding width; z_1 is the system output tracking error; z_2 is the difference between the actual state x_2 and the virtual state x_{2eq} ; \hat{z}_2 is the difference between \hat{x}_2 and x_{2eq} ; k_1 is a positive feedback gain.

According to Laplace transform, the third equation in (11) can be

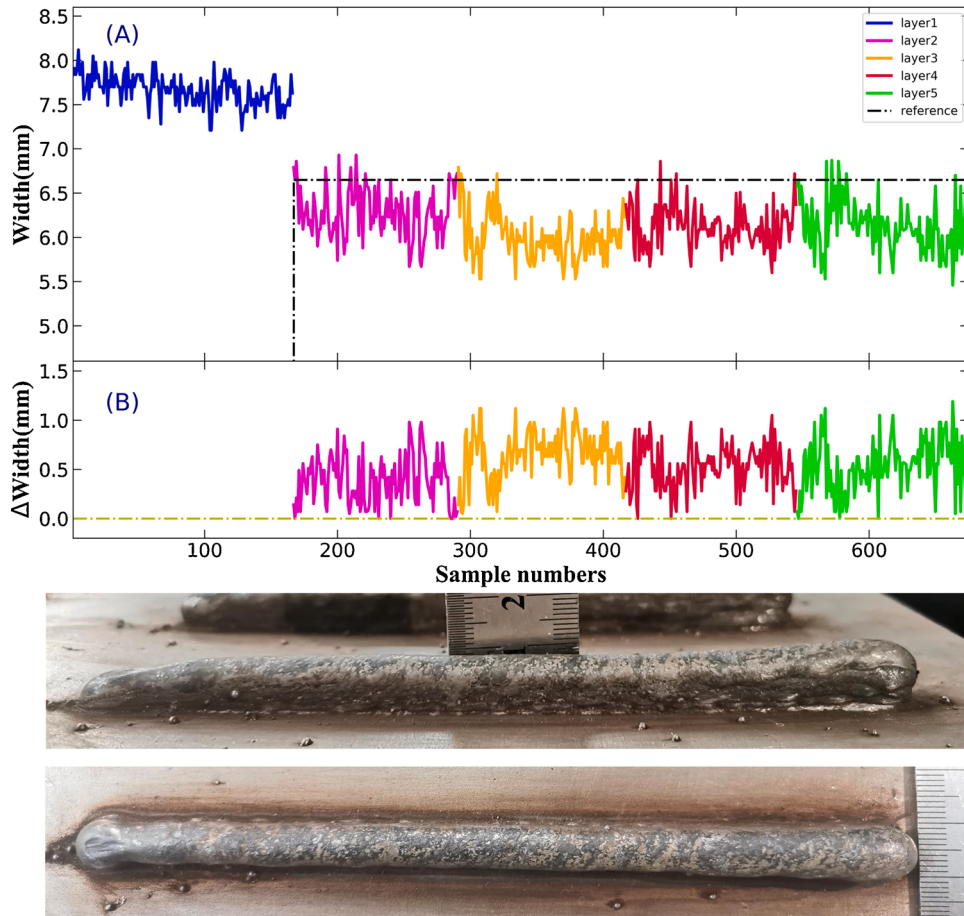


Fig. 15. Comparison of actual width of different layers.

Table 4
Analysis of different layer width results.

	2 nd layer	3 rd layer	4 th layer	5 th layer	Average
MAE(mm)	0.3915	0.6573	0.5267	0.5272	0.5257
RMSE(mm)	0.4627	0.7015	0.5737	0.5942	0.5829

rewritten as $\frac{z_1(s)}{z_2(s)} = \frac{1}{k_1 s + 1}$. In view of $k_1 > 0$, z_1 will converge to zero while z_2 converges to zero. Therefore, the derivative of z_2 can be derived by

$$\dot{z}_2 = \dot{x}_2 - \dot{x}_{2eq} = k_p u/a - bx_2/a - x_1/a + x_3 - \dot{x}_{2eq} \quad (12)$$

Based on (12), the control input u can be designed as

$$u = \frac{a}{k_p} (b\hat{x}_2/a + \hat{x}_1/a - \hat{x}_3 + \hat{x}_{2eq} - k_2\hat{z}_2) \quad (13)$$

where $\hat{x}_{2eq} = \ddot{x}_{1d} - k_1\hat{z}_1$.

Substituting (13) into (12), the dynamic of z_2 can be expressed as

$$\dot{z}_2 = -k_2\hat{z}_2 + b\tilde{x}_2/a + \tilde{x}_1/a - \tilde{x}_3 + \tilde{x}_{2eq} = -k_2z_2 + N(\tilde{x}_1, \tilde{x}_2, \tilde{x}_3) \quad (14)$$

where $\tilde{x}_{2eq} = \hat{x}_{2eq} - \dot{x}_{2eq}$; $N(\tilde{x}_1, \tilde{x}_2, \tilde{x}_3) = b\tilde{x}_2/a + \tilde{x}_1/a - \tilde{x}_3 + \tilde{x}_{2eq} - k_2\tilde{x}_2$.

Thus, based on the observer dynamics (9), the controller dynamics (11) and (14), the ultimately bounded tracking performance of the presented ADRC controller can be ensured, whose detailed proof procedure can be referred to [46].

4.4. Simulation verification

To attest the validity of the proposed method, two conditions including with disturbances and without disturbances are considered in the following simulation verification. The desired welding width is set as 6.65 mm. The proposed controller gains are selected as $k_1 = 5$, $k_2 = 5$, $w_0 = 10$.

Case 1: Without Disturbances

For this case, the welding width tracking and control current are given in Fig. 11. As seen, the actual welding width converges to the desired width quickly and eventually remains at the desired width 6.65 mm. The control current ultimately stabilizes at a constant value 191.6 A. The estimation of x_2 is presented in Fig. 12, which shows that the estimated state can well track the actual state and demonstrates the effectiveness of the constructed ESO.

Case 2: With Disturbances

In this case, the disturbance is added to simulate the effect of model identification error. Since the disturbance can be estimated by the designed ESO and compensated in the ADRC control design, there is no significant influence on the welding width tracking performance (see Fig. 13), which means that the proposed ADRC makes the system robust against the disturbance effect. Meanwhile, the state estimation in this case is shown in Fig. 14.

5. Experiment and analysis

In this paper, based on the non-pulsed direct current and the single-

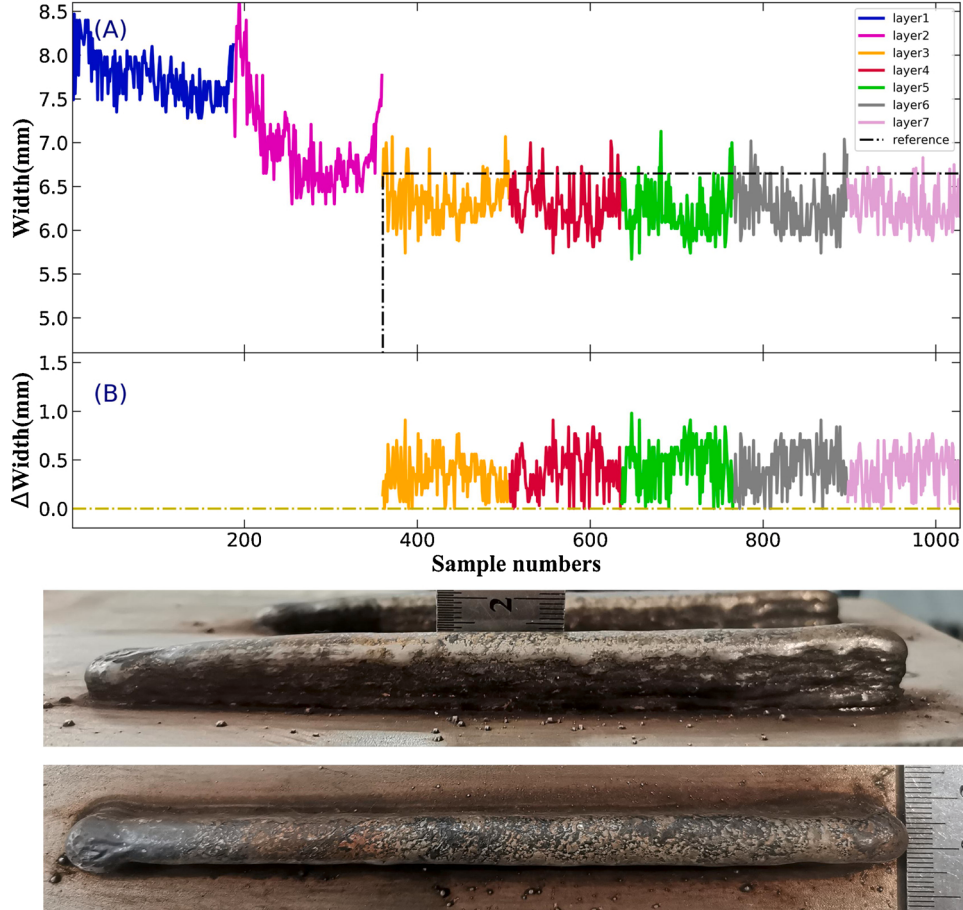


Fig. 16. Comparison of different layer width results in robustness test.

Table 5
Analysis of different layer width results in robustness testing.

	3 rd layer	4 th layer	5 th layer	6 th layer	7 th layer	Average
MAE(mm)	0.3504	0.3959	0.4524	0.4181	0.3844	0.4002
RMSE (mm)	0.3991	0.4515	0.5130	0.4732	0.4390	0.4552

pass multi-layer AM of stainless steel, the changes in width of deposited layer melt pool in WAAM process are monitored and controlled. The stacked method in this paper is co-deposition. The specific experimental parameters are shown in [Table 3](#).

The width and forming results of the first layer will affect the spreading and forming of the subsequent layers. Therefore, we use 312A current welding for the first layer (not controlled), and then use the control method in this paper to weld the next two to five layers. The target weld width is 6.65 mm and the results are shown in [Fig. 15](#). The data analysis results are shown in [Table 4](#).

The forming result shows that the second layer has the best control effect, and the width of the three to five layers is stable, but slightly lower than the target value. The average value of mean absolute error (MAE) for the second to fifth layers is 0.5257 mm, and the average value of root mean square error (RMSE) is 0.5829 mm. The calculation formulas are [\(15\)](#) and [\(16\)](#).

$$MAE = \frac{1}{m} \sum_{i=1}^m |w_i - \hat{w}_i| \quad (15)$$

$$RMSE = \sqrt{\frac{1}{m} \sum_{i=1}^m (w_i - \hat{w}_i)^2} \quad (16)$$

Where, m is the quantity, i is the number of times, w is the true value, and \hat{w} is the predicted value.

To further verify the robustness of algorithm, we use the first two layers of non-control (the first layer current is 312A, the second layer current is 320A) during the experiment, and the subsequent three to seven layers of control. The experimental results are shown in [Fig. 16](#), and the specific data analysis is shown in [Table 5](#).

The average value of MAE for the third to seventh layers is 0.4002 mm, and the average value of RMSE is 0.4552 mm. The maximum error is less than 1 mm, which is acceptable accuracy.

6. Conclusion

This paper first builds a melt pool vision sensor system to collect single-bead and multi-layer melt pool images in WAAM. A melt pool segmentation network named EPNet is proposed to segment the melt pool and extract its width. Finally, an ADRC algorithm is designed to realize the real-time control of the weld width in the WAAM process. There are three specific points as follows:

- (1) EPNet melt pool segmentation network uses ERFNet as the backbone network, and adds PPM to integrate the features of multi-scale depth images. And in the training process, the method of degenerate learning rate is used to prevent over-fitting and improve the accuracy of segmentation.
- (2) In order to improve the generalization ability of the network, before the data is sent to the network, data augmentation is performed on the melt pool image and label. It includes rotation, scaling and clipping, which make the network model more robust.
- (3) A WAAM-based ADRC algorithm is designed to adjust the welding current during the WAAM process to make the weld forming width reach the target value. Firstly, the target width is set, and then the width of the melt pool is obtained according to the real-time image of the melt pool. The controller changes the welding

current through the obtained width, so that the welding seam width reaches the target value.

The experimental results show that the designed control algorithm can guarantee the satisfactory control accuracy of melt pool width. The WAAM-based control algorithm proposed in this paper still needs to expand multi-process parameter testing, which is the main problem to be solved in the future.

Declaration of Competing Interest

The authors report no declarations of interest.

Acknowledgments

This work is supported by the National Natural Science Foundation of China (61727802, 61971227); Fundamental Research Funds for the Central Universities (30920031101); Jiangsu Provincial Key Research and Development Program (BE2018126).

References

- [1] Jiang J, Newman S, Zhong R. A review of multiple degrees of freedom for additive manufacturing machines. *Int J Comput Integr Manuf* 2020;34(2):195–211.
- [2] Jiang J, Xu X, Xiong Y, Tang Y, Dong G, Kim S. A novel strategy for multi-part production in additive manufacturing. *Int J Adv Manuf Technol* 2020;109:1237–48.
- [3] Jiang J, Xiong Y, Zhang Z, Rosen D. Machine learning integrated design for additive manufacturing. *J Intell Manuf* 2020;1–14.
- [4] Ge J, Lin J, Lei Y, et al. Location-related thermal history, microstructure, and mechanical properties of arc additively manufactured 2Cr13 steel using cold metal transfer welding. *Mater Sci Eng A* 2018;715:144–53.
- [5] Sarvankar S, Yewale S. Additive manufacturing in automobile industry. *Int J Res Aeronaut Mech Eng* 2019;7(4):1–10.
- [6] Liu R, Wang Z, Sparks T, Liou F, Newkirk J. Aerospace applications of laser additive manufacturing. *Laser Addit Manuf* 2017;13:351–71.
- [7] Yu C, Jiang J. A perspective on using machine learning in 3D bioprinting. *Int J Bioprinting* 2020;6(1):4–11.
- [8] Hsaelhuhn A, Wijnen B, Anzalone G, Sanders P, Pearce J. In situ formation of substrate release mechanisms for gas metal arc weld 3-D printing. *J Mater Process Technol* 2015;226:50–9.
- [9] Frazier William E. Metal additive manufacturing: a review. *J Mater Eng Perform* 2014;23:1917–28.
- [10] Stelia aerospace use WAAM build an airplane fuselage. Available from: <http://www.aerospace-technology.com/news/stelia-aerospace-develops-3d-printed-demonstrator-fuselage-panels/>.
- [11] Naval group and centrale nantes use WAAM to 3D print the world's first hollow propeller blade. Available from: <https://3dprintingindustry.com/news/navalgroup-and-centrale-nantes-use-waam-to-3d-print-the-worlds-first-hollow-propeller-blade-148700/>.
- [12] Joris Laarman lab designed MX3D Bridge. Available from: <https://mx3d.com/projects/mx3d-bridge/>.
- [13] Yang D, Wang G, Zhang G. Thermal analysis for single-pass multi-layer GMAW based additive manufacturing using infrared thermography. *J Mater Process Technol* 2017;244:215–24.
- [14] Wang Q, Jiao W, Wang P, Zhang Y. A tutorial on deep learning-based data analytics in manufacturing through a welding case study. *J Manuf Process* 2021;63:2–13.
- [15] Zhang Y, Wang Q, Liu Y. Adaptive intelligent welding manufacturing. *Weld J* 2021;100(1):63–83.
- [16] Du Q, Chen S, Lin T. Inspection of weld shape based on the shape from shading. *Int J Adv Manuf Technol* 2006;27(7–8):667–71.
- [17] Shen J, Zhao Z, Han J, Zhang Y. Dual-band welding speed monitoring method based on deep learning. Proceedings of the 2018 the 2nd International Conference on Video and Image Processing 2018:213–7.
- [18] Wu D, Chen H, Huang Y, Chen S. Online monitoring and model-free adaptive control of weld penetration in VPPAW based on extreme learning machine. *IEEE Trans Industr Inform* 2019;15:2732–41.
- [19] Kwon O, Kim H, Ham M, Kim W, Kim G, Cho J, et al. A deep neural network for classification of melt-pool images in metal additive manufacturing. *J Intell Manuf* 2020;31:375–86.
- [20] Huang Y, Xiao Y, Wang P, Li M. A seam-tracking laser welding platform with 3D and 2D visual information fusion vision sensor system. *Int J Adv Manuf Technol* 2013;67(1–4):415–26.
- [21] Bacioiu D, Melton G, Papaelias M, Shaw R. Automated defect classification of Aluminium 5083 TIG welding using HDR camera and neural networks. *J Manuf Process* 2019;45:603–13.
- [22] Xia C, Pan Z, Polden J, Li H, Xu Y, Chen S, et al. A review on wire arc additive manufacturing: monitoring, control and a framework of automated system. *J Manuf Syst* 2020;57:31–45.

- [23] Li F, Chen S, Wu Z, Yan Y. Adaptive process control of wire and arc additive manufacturing for fabricating complex-shaped components. *Int J Adv Manuf Technol* 2018;96:871–9.
- [24] Xiong J, Yin Z, Zhang W. Closed-loop control of variable layer width for thin-walled parts in wire and arc additive manufacturing. *J Mater Process Technol* 2016;233:100–6.
- [25] Xia C, Pan Z, Zhang S, Polden J, Wang L, Li H, et al. Model predictive control of layer width in wire arc additive manufacturing. *J Manuf Process* 2020;58:179–86.
- [26] Liu Y, Zhang Y. Model-based predictive control of weld penetration in gas tungsten arc welding. *Control Syst Technol* 2014;22:955–66.
- [27] Liu Y, Zhang Y. Control of 3D weld pool surface. *Control Eng Pract* 2013;21(11):1469–80.
- [28] Ma T, Liu J, Du F, Chen N. Research on vibration image segmentation based on improved Otsu method. *Electron Opt Control* 2019;26: 11-15+31.
- [29] Yu H, Mu P. Application of adaptive canny algorithm in edge detection of steel plate defects. *Soft Guide* 2018;17:175–7.
- [30] Chen Z, Li Y, Chen X, Yang C, Gui W. Texture and edge detection of metal images under high temperature and dynamic solidification conditions. *J Cent South Univ* 2018;25:1501–12.
- [31] Lei K, Qin X, Liu H, Ni M. Edge extraction of wide-layer laser cladding pool based on local active contour model. *J Optoelectron Laser* 2018;29:516–22.
- [32] Bai Y, Lou Y, Gao F, Wang S, Wu Y, Duan L. Group sensitive triplet embedding for vehicle reidentification. *IEEE Trans Multimedia* 2018;20:2385–99.
- [33] Ren S, He K, Girshick R, Sun J. Faster R-CNN: towards real-time object detection with region proposal networks. *Adv Neural Inf Process Syst* 2015:91–9.
- [34] Guo X, Chen L, Shen C. Hierarchical adaptive deep convolution neural network and its application to bearing fault diagnosis. *Measurement* 2016;93:490–502.
- [35] Long J, Shelhamer E, Darrell T. Fully convolutional networks for semantic segmentation. *IEEE Trans Pattern Anal Mach Intell* 2017;39:640–51.
- [36] Badrinarayanan V, Kendall A, Cipolla R. SegNet: a deep convolutional encoder-decoder architecture for image segmentation. *IEEE Trans Pattern Anal Mach Intell* 2017;39:2481–95.
- [37] Paszke A, Chaurasia A, Kim S, Culurciello E. ENet: a deep neural network architecture for real-time semantic segmentation. *Comput Vision Pattern Recogn* 2016.
- [38] Romera E, Alvarez J, Bergasa L. ERFNet: efficient residual factorized ConvNet for real-time semantic segmentation. *IEEE Trans Intell Transp Syst* 2017;1:1–10.
- [39] Yu W, Long H. Remote sensing image building segmentation method based on deep convolution network. *Comput Technol Dev* 2019;6:1–6.
- [40] He K, Zhang X, Ren S, Sun J. Deep residual learning for image recognition. *The IEEE Conference on Computer Vision and Pattern Recognition* 2016:770–8.
- [41] Yu F, Koltun V. Multi-scale context aggregation by dilated convolutions. *Proceedings of 4th International Conference on Learning Representations 2016*.
- [42] Zhao H, Shi J, Qi X, Wang X, Jia J. In: *Pyramid Scene Parsing Network*; 2016.
- [43] Wei S, Ji S, Lu M. Toward automatic building footprint delineation from aerial images using CNN and regularization. *IEEE Trans Geosci Remote Sens* 2020;58:2178–89.
- [44] Kang X, Gao G, Hao Q, Li S. A coarse-to-fine method for cloud detection in remote sensing images. *IEEE Geosci Remote Sens Lett* 2019;16:110–4.
- [45] Chen H, Li Y, Tian H, Zhang F, Guo Q. Improvement of regional-scale winter wheat growth modeling with sub-pixel information. *Chin J Ecol* 2018;37(7):2221–8.
- [46] Yao J, Jiao Z, Ma D. Extended-state-observer-based output feedback nonlinear robust control of hydraulic systems with backstepping. *IEEE Trans Ind Electron* 2014;61(11):6285–93.
- [47] Yao J, Deng W. Active disturbance rejection adaptive control of uncertain nonlinear systems: theory and application. *Nonlinear Dyn* 2017;89:1611–24.